

# An Analysis Framework for Understanding Deep Neural Networks Based on Network Dynamics

Yuchen Lin,<sup>\*</sup> Yong Zhang,<sup>\*</sup> Sihan Feng, and Hong Zhao<sup>†</sup>  
*Department of Physics, Xiamen University, Xiamen 361005, China*  
(Dated:)

Advancing artificial intelligence demands a deeper understanding of the mechanisms underlying deep learning. Here, we propose a straightforward analysis framework based on the dynamics of learning models. Neurons are categorized into two modes based on whether their transformation functions preserve order. This categorization reveals how deep neural networks (DNNs) maximize information extraction by rationally allocating the proportion of neurons in different modes across deep layers. We further introduce the attraction basins of the training samples in both the sample vector space and the weight vector space to characterize the generalization ability of DNNs. This framework allows us to identify optimal depth and width configurations, providing a unified explanation for fundamental DNN behaviors such as the "flat minima effect," "grokking," and double descent phenomena. Our analysis extends to networks with depths up to 100 layers.

A fundamental question in understanding deep neural networks (DNNs) revolves around their superior performance compared to shallow networks [1–3]. Despite often being over-parameterized, DNNs generally generalize well [4–6]. Significant strides have been made in elucidating this phenomenon [7, 8], with notable theories emerging such as the Information Bottleneck theory [9–12]. This theory provides a theoretical framework to understand how DNNs process and compress information layer by layer. Another pivotal theory is the "Flat Minima Hypothesis," which correlates the geometry of the loss surface with the generalization capabilities of neural networks [13–16]. Specifically, the former focuses on the compression of redundant information, while the latter suggests that flat minima, which are less susceptible to overfitting, are associated with superior generalization. In particular, it has been proven, by establishing a Fokker-Planck equation, that the flatness of the overall loss landscape increases during the learning process and attains a higher value when performing the stochastic gradient descent (SGD) algorithm with a smaller sample batch size [15–18]. Despite these general insights, the precise mechanisms and learning dynamics underlying DNNs remain elusive.

Due to the complexity of general DNNs, many theoretical studies focus on simplified scenarios to derive analytical results. For instance, some research linearizes the models [19–22], while others analyze shallow networks [23–25]. Whether these approaches based on linear models and shallow networks can fully capture the intrinsic advantages of nonlinear neurons in deep networks remains an open question. Furthermore, there are two key common issues that need to be clarified. The first is that previous studies often treat the learning model as a unified entity, whereas it is well-known that the linear summation and nonlinear activation are still the basic computing processes at the single neuron level. We should thus, in principle, relate the properties of DNNs to the behaviors of single neurons. The second is that

a learning model is indeed a dynamical map that maps inputs to outputs. In particular, the layers of a DNN can be considered as an iterative process of dynamical systems. Therefore, dynamical theories should be able to be utilized for understanding the learning dynamics.

Additionally, several intriguing phenomena have been observed in the realm of learning models, yet these have not been systematically linked to their underlying mechanisms. For instance, why do certain models initially exhibit behavior akin to linear neural networks (LNNs) before transitioning to nonlinear neural networks (NNNs) [25, 26]? Under what conditions does pruning deep layers Will not significantly affect model outcomes [27–32]? And why are residual connections crucial in constructing deep neural networks (DNNs) [33–37]? The superiority of these connections is uncertain; do they merely mitigate the vanishing gradient problem to facilitate deep network training, or do they also positively impact network accuracy? Furthermore, what is the general mechanism behind grokking and double descent [38–42]? Grokking refers to a sudden performance jump after a prolonged plateau, observed across various scenarios. Double descent, conversely, describes a phenomenon where the test error initially decreases, then increases, and finally decreases again as model complexity increases. Unraveling these phenomena could pave the way for improved model design and regularization strategies.

In this paper, we aim to understand the learning dynamics of neural networks by establishing a framework that encompasses three fundamental dimensions: information extraction, information transformation, and generalization ability. This framework is grounded in the basic building blocks of neural networks: single-neuron functions and the attraction basins of learning models. We employ the classification task as an exemplary case to illustrate our points, although the generalization of our findings to other scenarios is straightforward.

In the following section, we adopt a novel approach to categorizing neurons. Rather than classifying them

based on the linearity or nonlinearity of their transfer functions, we categorize neurons into two distinct modes according to whether their transformation functions preserve the order of inputs. This distinction allows us to gain a deeper understanding of how neurons process and transform information. We then introduce two types of attraction basins: one in the sample vector space and another in the weight vector space. These attraction basins play a crucial role in determining the behavior and performance of neural networks during the learning process.

In Section III, we delve deeper into the characteristics of these two modes of neurons in hidden layers. We introduce several quantities to describe the distribution and evolution of these neurons, which can help identify the linearity of network layers and the degree of linear separability of sample vectors after transformation through previous layers. These quantities also provide criteria for layer pruning, which is essential for optimizing the structure of DNNs.

In Section IV, we reveal the learning dynamics of shallow learning models, illustrating the roles of the two neuron modes. We then turn our attention to DNNs in Section V. We demonstrate that DNNs can self-organize into a standard structure, with nonlinear layers in the earlier stages and linear layers in the later stages. Using neuron mode and attraction basin analysis, we identify the optimal depth and width, the optimal batch size and the optimal learning rate for training DNNs. We emphasize that the dependence of the two types of attraction basins on depth and width differs, while on the batch size and the learning rate is consistent. Furthermore, we provide criteria for pruning, discuss the connection of attraction basins to the flat minima effect, and explain the superiority of DNNs with residual connections. We also offer explanations for phenomena such as grokking and double descent within the framework of our analysis. Finally, in the last section, we conclude our findings and provide remarks on the implications of our work.

1.

## BASIC CONCEPTS AND METHODS

**Models.** To illustrate our framework, we consider two types of DNNs. The first is a fully connected DNN, described mathematically by the following equations:

$$\begin{aligned} x_{i_l}^{(l)} &= f(h_{i_l}^{(l)}), \\ h_{i_l}^{(l)} &= \sum_{i_{l-1}=1}^{N_{l-1}} w_{i_l i_{l-1}}^{(l)} x_{i_{l-1}}^{(l-1)}, \end{aligned} \quad (1)$$

Here,  $x_{i_l}^{(l)}$  represents the output of the  $i_l$ -th neuron in the  $l$ -th layer, and  $h_{i_l}^{(l)}$  denotes the local field of the same

neuron. The weight  $w_{i_l i_{l-1}}^{(l)}$  connects the  $i_{l-1}$ -th neuron in the  $(l-1)$ -th layer to the  $i_l$ -th neuron in the  $l$ -th layer. The function  $f(\cdot)$  serves as the neuron's transfer function. The number of neurons in the  $l$ -th layer is denoted by  $N_l$ .

The second DNN model we consider utilizes residual connections. In this case, every two layers, the first equation in Eq. (1) is modified to:

$$x_{i_l}^{(l)} = x_{i_{l-2}}^{(l-2)} + f(h_{i_l}^{(l)}), \quad (2)$$

where the residual connection allows the outputs of one layer to be directly added to the outputs of the layer two steps ahead. This modification introduces a skip connection that helps in preserving the information flow through the network, potentially improving its learning capabilities.

**Modes of Neurons.** Our point of view to information encoding is as follows. A weight vector  $\mathbf{w}$  projects a sample vector  $\mathbf{x}^\mu$  onto a local field  $h(\mu) = \mathbf{w} \cdot \mathbf{x}^\mu$ , which serves as the input to a neuron. The sequence  $h(\mu)$  with  $\mu = 1, 2, \dots, P$  represents the local fields of this neuron for all  $P$  samples. The ordering of this sequence and the spatial intervals among  $h(\mu)$  values encode the distinct relationships and information among the samples along this particular weight vector. Different neurons capture different aspects of the information by employing different weight vectors.

The input layer plays a pivotal role in information extraction. In principle, the number of weight vectors in this layer must exceed the dimensionality (refers to the effective dimension) of the samples to ensure that the weight matrix remains non-degenerate. Beyond this threshold, any new weight vectors will no longer be independent. To maximize information extraction, the weight vectors should ergodically span all directions in the weight vector space. This requirement renders the scenario depicted in Fig. 1(a) preferable to the one shown in Fig. 1(b).

Subsequently, the neural transfer function transforms the sequence into the neuron's outputs, aiming to minimize the loss. Typically, the goal is to activate the corresponding neuron for each class in the output layer. To achieve this, a neuron in the hidden layer should maximize the outputs for samples belonging to a specific class. There are two qualitative modes to accomplish this:

1. **Order preserve mode (OPM):** This mode preserves the order of the inputs, resulted by the linear transfer function as shown in Fig. 1(c). It can be also resulted by nonlinear Tanh-type transfer functions operating in the nearly linear region. Even though implemented by a nonlinear function, the operation is essentially linear in nature.

2. **Non-order preserve mode (NPM):** This mode alter the order of the inputs. This can be achieved by a single neuron using Gauss-type transfer functions, as depicted

in Fig. 1(d), or through combinations of neurons using Tanh-type transfer functions, as shown in Fig. 1(e). This mode allows a local field at any position in the sequence to be maximized, and it is an inherently nonlinear operation.

The expected outcome of these neural processing modes is to maintain information without reduction and to achieve effective separation of different classes. This entails clustering similar samples together while ensuring that different classes are well-separated. Each individual neuron needs to contribute to this task, i.e., to maximize the outputs of specific samples. However, to achieve this purpose, the OPM needs to direct the weight vectors towards specific directions in order to project the local fields of the desired samples towards the ends of the sequence, thereby obtaining output values as large as possible, resulting in the scenario depicted in Fig. 1(b). This convergence towards specific directions may not only reduce the ability to extract information from potential directions but may also increase the overlap of  $h(\mu)$  among samples from different classes.

On the other hand, the convergence of weight vectors is not necessary for performing the NPM. This results in greater freedom to extract information from a wider range of weight vector directions, as demonstrated by the scenario shown in Figure 1(a). However, NPM neurons exhibit high input-output sensitivity, whereas OPM neurons offer the advantage of minimal sensitivity, characterized by a zero second-order derivative.

An optimal learning model should therefore leverage an optimal combination of neurons operating in both modes. By combining the stability and minimal sensitivity of OPM neurons with the flexibility and information extraction capabilities of NPM neurons, the model can achieve better performance in terms of both accuracy and robustness. This balance is crucial for developing effective neural networks that can handle complex and varied datasets.

**Attraction basins.** Our second key tool is the introduction of attraction basins to characterize the network dynamics. Attraction basins are fundamental concepts in nonlinear dynamical systems. Considering the layers of a DNN as iterative operations, this concept can be extended to DNNs. Here, we define the attraction basin of a training sample in two vector spaces.

First, after achieving 100% training accuracy, we add random variations to a training sample and check whether the learned model can correctly classify these variations into the same class as the original sample. By plotting the average accuracy of the noised training set as a function of noise amplitude, one should observe a transition from 100% accuracy to an accuracy of random noise samples. The noise amplitude threshold at which this transition occurs can be used as a metric for the average size of the attraction basin in the sample vector space. This size measures the generalization ability of

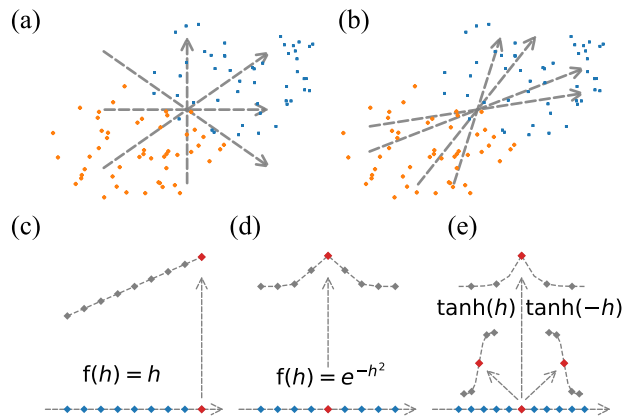


FIG. 1. Illustration of weight vector distributions induced by the OPM (a) and the NPM (b). (c) Represents the way of extracting information using the OPM, (d) shows extraction using the NPM of Gaussian function, and (e) depicts extraction using the NPM of the ReLU function.

the model to variations in the input data.

Another way to define the attraction basin is by adding noise to the weights of the network and checking whether a training sample can still be correctly classified. The attraction basin size defined in the weight vector space measures the stability of the network's structure or its robustness to variations in the weights. It has been shown that there is a dual relationship between variations in the weights and variations in the samples [reference to relevant literature]. We reveal in the following sections that the sizes of the two attraction basins have different dependencies on the depth and width of the network, and there is a solid correlation between the flat minima effect and the basins of attraction will be established.

## QUANTITIES FOR ANALYZING THE LEARNING PROCESS AND DNN STRUCTURE

Samples are transformed layer by layer through a DNN, ultimately becoming linearly separable in the output layer. This is the general paradigm of DNNs. To characterize the linear separability of sample vectors from a deep layer to the output layer, we introduce a linear perceptron (LP) to replace the section of the DNN from the  $l$ -th layer onward. Specifically, the LP is trained using the sample set  $(\mathbf{x}^{(l)}(\mu), \mathbf{y}(\mu))$ ,  $\mu = 1, \dots, P$ , where  $\mathbf{x}^{(l)}(\mu)$  represents the output of the  $l$ -th layer for the  $\mu$ -th sample, and  $\mathbf{y}(\mu)$  is the corresponding local fields from the last layer.

When the outputs of a hidden layer become well linearly separable, the LP can perform the classification task effectively, indicating that the section of the DNN after this layer can be replaced by a linear model. For simplicity, we construct the LP using a least squares op-

timization algorithm. The LP approach has been applied in previous studies [43–46].

To assess the linearity of the DNN from the  $l$ -th layer to the output layer, we introduce a linear map (L-map) by replacing the nonlinear transfer function  $f(h)$  after this layer with a linear function  $f(h) = h$ . The L-map, with a weight matrix defined as

$$\mathbf{W}^{\text{L-map}} = \mathbf{W}^{(l)} \cdot \mathbf{W}^{(l+1)} \dots \mathbf{W}^{(L)},$$

can replace the section of the network from the  $l$ -th layer onward when the network effectively behaves as a truly linear network. Here,  $\mathbf{W}^{(j)}$  represents the weight matrix of the  $j$ -th layer.

In this scenario, the L-map effectively acts as a linear perceptron, albeit one that is not trained independently but rather derived from the weights of the original DNN. Its purpose is to characterize the inherent linear structure of the DNN, providing insights into how well the network has learned to map inputs to outputs in a linearly separable manner.

To further characterize the proportion of OPM and NPM neurons, we introduce the ranking position distribution (RPD) as a quantitative tool. We first establish this concept on the basis of LNNs and extended to general DNNs. For a LNN,  $h_{i_{l-1}}^{(l-1)}(\nu)W_{ki}^{\text{L-map}}$  characterizes the contribution of the  $i_{l-1}$ -th neuron in the  $(l-1)$ -th layer to the  $k$ -th neuron (representing the  $k$ -th class) in the output layer through the L-map, when the  $\nu$ -th sample is inputted. We sort  $h_{i_{l-1}}^{(l-1)}(\nu)W_{ki}^{\text{L-map}}$  in the sequence  $h_{i_{l-1}}^{(l-1)}(\mu)W_{ki}^{\text{L-map}}$  with  $\mu = 1, 2, \dots, P$  to obtain its rank. The LNN only possesses the OPM mode, which needs to aggregate weight vectors towards specific directions to make  $h_{i_{l-1}}^{(l-1)}(\nu)W_{ki}^{\text{L-map}}$  as large as possible for a sufficient number of neurons. In such a case, the order of  $h_{i_{l-1}}^{(l-1)}(\nu)W_{ki}^{\text{L-map}}$  should be high, with the most ideal situation to rank ahead of all other classes of samples. To characterize this effect, we obtain the rank for each sample regarding to its target neuron, and then calculate the distribution of ranking positions across all neurons in the layer. A high probability density in the high-ranking region is expected if the training goal is achieved.

The OPM in a DNN with nonlinear transfer functions can similarly lead to a RPD with a high probability density in the high-ranking region, while the NPM is not directly related to the rank, as it can transform the local field at any position within the input sequence to achieve maximum output. Therefore, changes in the gradient or slope of the RPD can be used as a qualitative indicator to probe the proportions of OPM and NPM neurons in a deep layer. A steep gradient may suggest a higher proportion of OPM neurons, while a flatter gradient may indicate a higher proportion of NPM neurons.

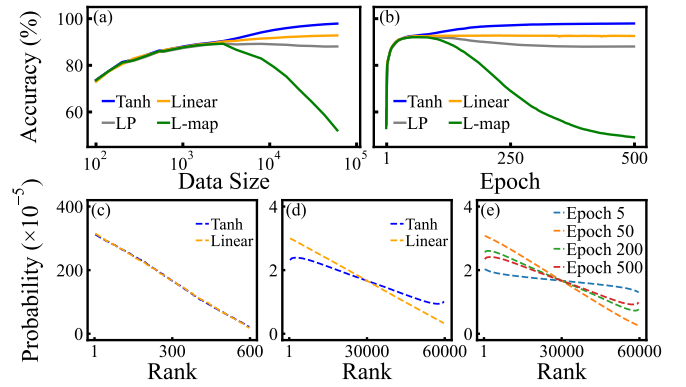


FIG. 2. (a) Accuracy as a function of training sample size. From top to bottom, the lines represent the NNN with Tanh function, the LNN, the LP, and the L-map. (b) Accuracy as a function of training time for a 60,000-sample training set, with the same ordering of lines as in (a). (c) RPDs for the NNN with Tanh function and the LNN trained with 600 samples. (d) RPDs for the NNN with Tanh function and the LNN trained with 60,000 samples. (e) Evolution of RPD for the NNN with Tanh function at different training times.

## APPLICATIONS TO SHALLOW NETWORKS

We first demonstrate how to utilize the quantities introduced in the previous section to analyze a 784-2048-10 neural network designed for handwritten digit recognition using the MNIST dataset [47]. This dataset comprises 60,000 training samples and 10,000 test samples, where each sample is represented as a  $28 \times 28$  bitmap. Figure 2(a) depicts the accuracy of the networks as a function of sample size. The accuracy for the NNN (employing the Tanh activation function), along with the accuracies of the LP and L-map derived from this NNN, are also presented. The LP is trained with the sample vectors as input and the network’s local field  $h^L(\mu)$  as output.

For small training sets, we observe that the four accuracy curves converge, indicating that the NNN behaves effectively as a LNN. Figure 2(c) displays the RPDs of the hidden layer for both the NNN with Tanh and the LNN, using 600 training samples. Notably, in this shallow network,  $h_{i_2}^{(2)}(\mu)W_{ki}^{\text{L-map}} = h_{i_2}^{(2)}(\mu)W_{ki_2}^{(2)}$ . The distributions exhibit a high probability in the high-ranking region and a low probability in the low-ranking region, suggesting that OPM neurons dominate the learning process. The precise alignment of the RPD curves for the LNN and Tanh-NNN confirms that this NNN is composed entirely of OPM neurons.

However, as the training set size increases, the accuracy curves deviate, indicating the significant activation of NPM neurons. The degree of separation between the Tanh-NNN and L-map curves quantifies the accuracy loss due to the linearization of the NNN with  $f(h) = h$ . Figure 2(d) reveals that the RPDs diverge markedly with



a training set size of 60,000, with the LNN exhibiting a steeper gradient. This confirms the activation of a substantial number of NPM neurons within the NNN.

The linearity of the NNN evolves throughout the training process. Figure 2(b) illustrates the accuracy as a function of training time using a 60,000-sample training set. Initially, the four accuracy curves overlap but gradually diverge as training progresses. Figure 2(e) displays the evolution of the RPD for the Tanh-NNN: the gradient increases initially, reaches a maximum, and then decreases towards the final state. This reflects that in the early stage of the network, learning occurs through OPM (confirmed by the consistency of the four curves), driving the weight vectors to concentrate in specific directions. Subsequently, NPM neurons are activated, and the weight vectors spread out in broader directions, thereby enabling the gradient descent of RPD. Therefore, for small, well-linearly separable training sets, the training goal may be achieved during the OPM learning phase, causing the neural network to retain its linear structure. Conversely, for larger training sets, if the training goal is not met during the OPM phase, NPM neurons are activated to extract information from a broader range of directions in the weight vector space. The transition from an OPM-dominated phase to a mixed phase of OPM and NPM neurons may occur as the number of training samples increases or as training progresses.

## APPLICATIONS TO DNNs

**The Standard Structure of DNNs.** In Figure 3, the results for DNNs with and without residual connections are presented in the first and second columns, respectively. Both DNNs utilize the ReLU transfer function. Figures 3(a) and 3(b) explore the depth dependence of accuracy when employing LP pruning (replacing later layers with the LP) and L-map pruning (replacing later layers with the L-map). These plots reveal that LP achieves effective pruning in much earlier layers, suggesting that samples become linearly separable after just a few layers. Conversely, L-map pruning becomes effective in later layers, indicating that the final sections of the DNN evolve into a pure LNN, equivalent to a linear perceptron.

Figures 3(c) and 3(d) exhibit RPDs for several representative layers of the two DNNs. It is observed that the RPD gradient increases with layer depth, confirming the decrease of NPM neurons with the depth. When L-map pruning becomes effective, the RPD gradients attain their maximum values, further confirming that the deeper layers transform into a LNN.

Figures 3(e) and 3(f) depict the evolution of the cosine distance between a sample vector  $\mathbf{x}^{(l)}(\mu)$  and the center vector of its class in the  $l$ -th layer as a function of network depth for the two DNNs. For clarity, only the first 100

samples of the digit "5" class are plotted. Additionally, the average cosine similarity between the center vectors of different classes is shown.

We observe that, in general, samples cluster towards the center of their respective classes as depth increases, while the center vectors of different classes become mutually orthogonal. This progression signifies that the network effectively organizes the representation space, enhancing class separability as depth increases. This effect has been previously documented in certain studies.

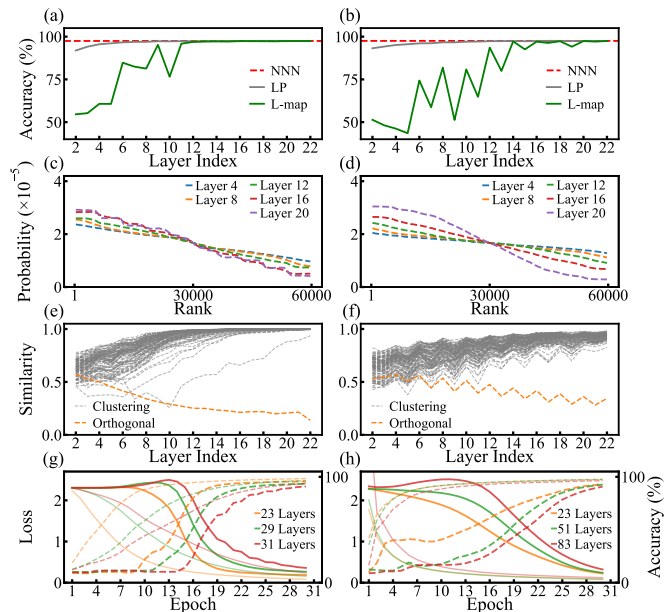


FIG. 3. Learning dynamics of DNNs with 22 hidden layers. Subfigures (a) and (b) display the accuracies achieved through LP and L-map pruning, respectively. The horizontal axis indicates the number of the starting layer, and the accuracies of the unpruned DNNs are provided as a reference. Subfigures (c) and (d) present the RPDs for selected hidden layers. Subfigures (e) and (f) depict the evolution of the cosine distance for the first 100 training samples of the digit "5", along with the average cosine distance among different classes. Subfigures (g) and (h) showcase the grokking and double descent phenomena, with the first column illustrating DNNs without residual connections and the second column depicting DNNs with residual connections.

Figures 3(g) and 3(h) illustrate the test loss, as well as the test and training accuracies, as functions of training time for DNNs with varying numbers of hidden layers. Both figures exhibit the grokking and double descent phenomena, which become increasingly pronounced as the number of hidden layers increases. The periodic oscillations observed in the second plot stem from the presence of residual connections, which are applied every two layers.

**The depth and width dependence of test accuracy.** In the following subsections, we present results only for DNNs without employing residual connections, as these phenomena and behaviors as qualitatively simi-

lar. In Figure 4(a), we show the test accuracy as a function of depth for various widths. The minimum number of hidden layers required to achieve 100% accuracy on the 60,000 training samples is two. Therefore, the horizontal axis starts from the fourth layer. We observe that for a fixed width, the accuracy initially increases and then decreases with depth. For a fixed depth, the accuracy generally increases with width, and approximately converge to a universal curve. The maximum accuracy occurs for DNNs with approximately for 8-layer DNNs. Figure 4(b) plots the RPD for the first hidden layer using DNNs with widths of 128 for several depths. We see that, in the high rank region, the probability of 8-layer DNN is the lowest, mining that there achieves the highest ratio of NPM neurons with the depth.

**The depth and width dependence of attraction basins.** Figure 5(a) shows the average accuracy of noised training samples, and 5(b) shows the average accuracy of training samples under noised weights, as a function of noise amplitude for a 1024-layer DNN with different depth, respectively. The noise amplitude that transition from the 100% accuracy to 10% (on the random noise level) indicates the size of the average attraction basins. We see that the attraction basins on the sample vector space increase with the increase of depth initially but converge after the DNNs exceed about 8 layers. While the attraction basins on the weight-vector space decreases with the increase of depth initially but converge after also the DNNs exceed 8 layers.

We can similarly study the attraction-basin dependence on the width. we apply the noise amplitude that the accuracy is reduced to half to characterize the average size of attraction basins. Figure 5(c) plots the size of attraction basins on the sample vector space, and 5(d) plots the size of attraction basins on the weight vector space, as a function of DNN width for several depths, respectively. We see that, for a fixed depth, the attraction basin on the sample vector space (on the weight vector space) increases (decreases) firstly with the increase of width and then tends to converge. The converged width is around 400 but slightly dependence on the depth. While for a fixed width, the attraction basin on the sample vector space (on the weight vector space) increases (decreases) with the increase of depth.

Therefore, the two types of attractions have an opposite dependency relationship regarding depth and width. Furthermore, excessive depth or excessive width (not shown here) can both lead to significant fluctuations. In deed, if the network is too wide or too deep, the standard structure shown in Figure 3(a) will no longer be maintained.

**The learning dynamics of DNNs.** The above results reveal a general picture of how a DNN achieves learning. It evolves to a self-organized standard structure, with a high ratio of NPM neurons in the earlier layers and a decreased ratio in the later layers; The last

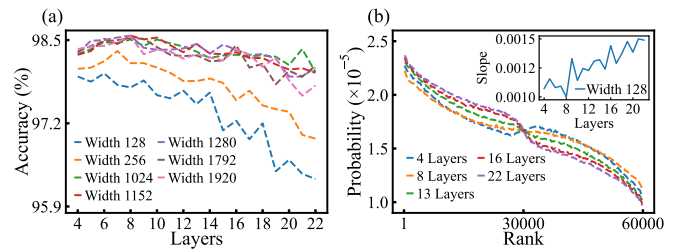


FIG. 4. (a) Test accuracy as a function of depth for various widths. (b) Gradient of the RPDs as a function of depth for DNNs with widths of 128 and 2048.

section may transit to pure OPM neurons.

The attraction basin in the sample vector space increases with the increase of depth and width. This is a significant advantage of DNNs which enhances the generalization. However, the attraction size converges to a fixed value when the depth exceeds a threshold. This threshold is consistent with the depth for maximum accuracy (Fig.4(a)) and the depth where the L-map pruning can be performed (Fig.3(a)). It is also consistent with the depth inducing the highest ratio of NPM neurons in the first layer (Fig. 4(b)), which thus can encoding more information. The decrease of NPM neurons with the further increase of the depth also explains the phenomenon where, although the basin of attraction reaches saturation at greater depths, the accuracy decreases. This demonstrates that the amount of information extracted, specifically the proportion of NPM neurons, is not equivalent to the control parameter for the basin of attraction. In addition, the basin of attraction remains unchanged in the later section of DNN with pure OPM neurons, and its expansion is completed in the NPM layers. The NPM is thus crucial for DNNs.

The increase in accuracy with the width also indicates the crucial role of the first layer in encoding information. In principle, the dimensionality of the weight vectors must reach the dimensionality of the sample vectors (here referring to the effective dimensionality, as sample vectors generally have redundant dimensions) in order to project the vector information without degeneracy. Therefore, accuracy rapidly increases with width and then reaches a saturation value, see Fig. 6(c).

The attraction basin in the weight vector space decreases with the increase of depth and width. Therefore, though increasing the width and depth is both beneficial for expanding the basin of attraction of samples and achieve a better generalization, but indeed detrimental to the stability of the DNNs. Therefore, from the perspective of the basin of attraction, a DNN should have an optimal balance between width and depth.

**The attraction basins and the flat minima hypothesis.** Many relevant phenomena can be understood based on the variations of attraction basins and neuron modes. We first show the connection of the attraction

basin in the weight vector space and the flat minima effect. We have seen that over-increasing in depth and width indeed compromises structural stability. However, we show that techniques employed in DNNs, such as selecting a smaller sample batch size, employing an appropriate learning rate, and applying suitable regularization, can all contribute to expanding the basin of attraction in both the sample vector space and the weight space. This expansion enables the DNNs to maintain their superior generalization capability while gaining structural stability.

In Figs. 6(a) and 6(b), we present the accuracy of training samples with added noise to the inputs and weights, respectively, as a function of noise amplitude for various batch sizes used in the adam algorithm. These results are for DNNs with a depth of 12 and a width of 1024. We observe that, in both cases, the size of the attraction basin increases as the batch size decreases. Specifically, the test accuracy rises from 98.3% to 98.9% when the batch size is reduced from 30,000 to 300 (see the insert).

In Figs. 6(c) and 6(d), we demonstrate the dependence of the attraction basin on several learning rates. These results are for DNNs with a depth of 12, a width of 1024, and a batch size of 300. We see that the attraction basin increases as the learning rate decreases. The test accuracy rises from also 98.3% to 98.9% when the rate increases from 0.1 to 0.5 (see the insert). However, it should be noted that while the attraction basin expands, the accuracy does not necessarily increase monotonically with the further increase in the learning rate; rather, it peaks at an optimal learning rate.

Since in both case the changes in attraction size is much more sensitive in the weight vector space than in the sample vector space, we can attribute the increase in accuracy to the expansion of the attraction basin size in the weight vector space. This expansion should indicate an expansion of the range of flat minima.

**Explaining the grokking and double decent effects.** The grokking effect can be explained straightforwardly based on the attraction basin. The idea is that test samples can be considered noisy variations of the training samples. In the initial stage of training, the attraction basins of training samples have not yet been fully established, resulting in both training and test accuracies being at random noise levels. As training progresses, the attraction basins gradually form, leading to an increase in training accuracy. However, due to the smaller size of these basins, test samples may fall outside them, resulting in accuracy levels close to random samples. During this stage, the test loss remains at random noise levels without any decline. As training continues, the basins expand, allowing more test samples to fall within them, enabling correct classification. Therefore, one can predict that grokking, a sudden jump in test accuracy, may occur during the training process.

The grokking effect in shallow networks do can be re-

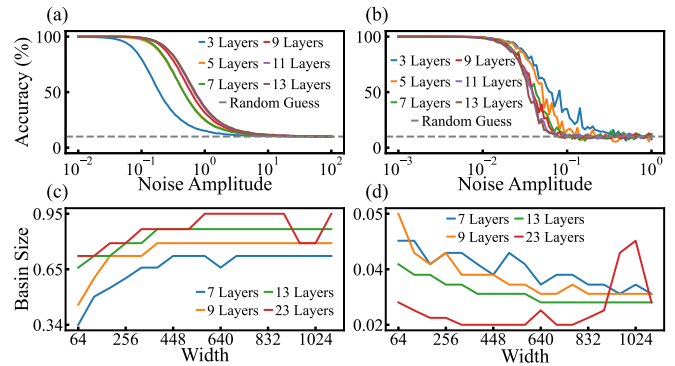


FIG. 5. The attraction basin and flat minima effect. (a) and (b) display the accuracy of training samples with added noise to the inputs and weights, respectively, as a function of noise amplitude for various batch sizes used in the SGD algorithm. The results are for DNNs with a depth of 12 and a width of 1024. (c) and (d) show the same metrics but for different learning rates, with a fixed batch size of 300. (e) and (f) illustrate the correspondence between the flatness of minima and the size of attraction basins in the weight vector space, respectively.

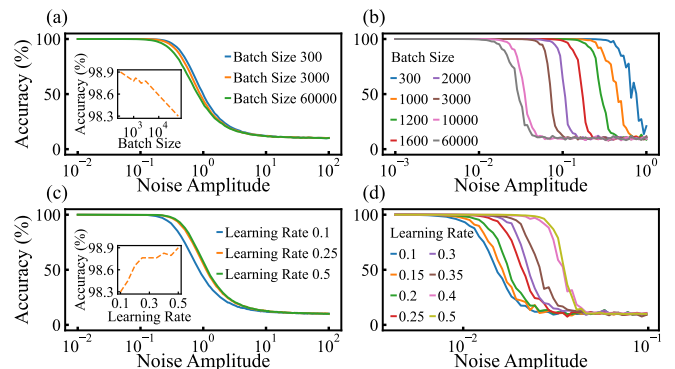


FIG. 6. The dependence of attraction basins on depth and width. (a) Displays the accuracy of training samples with added noise, as a function of noise amplitude. (b) Shows the accuracy of training samples when the weights are perturbed with noise, also as a function of noise amplitude. (c) Illustrates the attraction basins in the sample vector space for different network widths. (d) Demonstrates the attraction basins in the weight vector space, again for various network widths. Note that in (c) and (d), the dependence on width is shown for several different width values.

lated to the attraction basin in the sample vector space. To demonstrate this, we studied a 784-200-200-10 network, which exhibits a pronounced grokking effect [48]. In Figure 7(a), we reproduce the grokking phenomenon in this model, showing a notable delay in test accuracy compared to training accuracy. The accuracy of noised training samples with different noise amplitudes is also presented. We observe a clear transition with increasing noise amplitude. In Figure 7(b), we plot the accuracy of noised training samples and training samples with noised

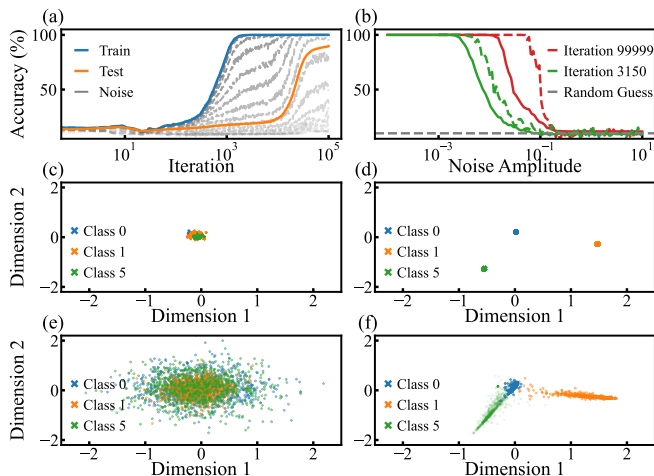


FIG. 7. Grokking Mechanism of DNNs. (a) Illustrates that grokking does not occur when the training mode of Batch Normalization is active. (b) Displays the change rate (indicated by dashed lines) of RPD for several deep layers as a function of training time. (c) and (d) Show two-dimensional projections of the digit "5" immediately before and after the grokking event, respectively.

weights at three stages: where both training and test accuracy are low, before grokking, and after grokking. For the first case, both accuracies are at noise levels, indicating that the attraction basins of training samples have not effectively formed. The transition from 100% accuracy to noise-level accuracy occurs around  $10^{-3}$  and  $10^{-2}$  for noised samples just before and after grokking, respectively. The transition for noised weights occurs slightly later. In this model, we thus can anticipate that grokking will occur for test samples, since the variation amplitude, relative to the training samples, is approximately  $10^{-2}$ .

We show that the grokking observed in Figure 7(a) do represents an abrupt change in the network's dynamic behavior with the expand of the attraction basin in sample vector space. We plot a pair of local fields of output-layer neurons (i.e., we select two neurons and plot their outputs as  $x$  and  $y$  coordinates) for test samples (Figure 7(c) and 7(d)) and training samples (Figure 7(e) and 7(f)) of "1," "2," and "3" before and after grokking, respectively. Before grokking, the projections of test samples are mixed and distributed across a vast region, far outside where the projections of training samples are distributed. After grokking, the projections of test samples overlap with those of training samples, indicating that most test samples have fallen within the attraction basins of training samples. Furthermore, before grokking, the distributions of training samples overlap with each other, while after grokking, the projections converge to small and mutually separated regions. These observations suggest a transition in network dynamics, similar to the case of asymmetric Hopfield neural networks [49], where a sharp transition from a chaotic phase to a memory phase occurs as

the attraction basins enlarge [50, 51].

However, the mechanisms underlying grokking in deep and shallow networks may differ. Comparing Figure 5(a) and Figure 7(b), we can observe that the noise level required to observe such a transition is significantly higher in the DNN than in the shallow network. Once the attraction basins are established, samples with a noise magnitude around one (note that the sample vectors are normalized in each layer) fall into the attraction basin. The test samples are typically small variations of the training samples, corresponding to a noise level of  $10^{-2}$ . Therefore, it can be inferred that grokking should not be observable in such a DNN under these conditions due to the depth leads to a huge basin of attraction in sample vector space.

The mechanism observed in Figure 3 has a distinct origin. We examine the algorithm we applied for training DNNs. It is found that Batch Normalization (BN) [52] behaves differently in the training and evaluation modes [53]. The training mode is used during the training of DNNs with training samples. In training mode, BN normalizes each layer using the mean and variance from the current mini-batch. The evaluation mode is used when evaluating test accuracy on test samples. In evaluation mode, BN uses a moving average of the mean and variance accumulated during training. Specifically, the updates follow the formulas:

$$\hat{\mu}_t = \alpha \hat{\mu}_{t-1} + (1 - \alpha) \mu_t$$

$$\hat{\sigma}_t^2 = \alpha \hat{\sigma}_{t-1}^2 + (1 - \alpha) \sigma_t^2$$

where  $\hat{\mu}_t$  and  $\hat{\sigma}_t^2$  are the moving average estimates used to normalize the test set, and  $\mu_t$  and  $\sigma_t^2$  are the mean and variance of the current training batch, with  $\alpha$  typically set to 0.9. This constitutes a significant perturbation to the weights. Meanwhile, as Figure 5(b) indicates, the average attraction basin in weight vector space is much smaller than that in sample vector space, as shown in Figure 5(a); it is around  $10^{-2}$ , which is comparable to the level of attraction basins in the case of shallow networks (see Figure 7). Therefore, the grokking observed in Figure 3 is attributed to the perturbations on the weights during the test process.

To confirm these arguments, we first replaced the evaluation mode with the training mode during the test process (i.e., using only the statistics from the current mini-batch during evaluation, by setting  $\alpha = 1$ ). Figure 6(c) confirms that the grokking disappears under these conditions. We then, in the evaluation mode, plotted a pair of local fields of output-layer neurons for both test and training samples, before (Figure 6(a)) and after (Figure 6(d)) the occurrence of grokking. We observe that before grokking, the projections of test samples are far from the projections of training samples, implying that the test samples are outside the attraction basins. After



grokking, however, the projections of test and training samples overlap, indicating that most test samples have fallen into the attraction basins.

Given that the evaluation mode with Batch Normalization is ubiquitous in typical DNN training programs, one can expect that this type of grokking may be commonly encountered. Additionally, other algorithms may similarly perturb the weights, potentially inducing grokking.

The attraction basin concept also explains why the test loss appears to remain almost unchanged before grokking (as shown in Figures 3(e) and 3(f)). This is because most test samples remain outside the attraction basins and thus do not contribute to the reduction of test loss. In Figure 3(a), we observe a phenomenon where the test loss may rise slightly before decreasing after grokking, especially when the DNN is sufficiently deep. This is known as the double descent phenomenon.

We argue that this rise is due to the extreme processing of the OPM during training. In Figure 6(b), we plot the changing rate of gradients of RPD of later layers as functions of training time. It is evident that the rise in test loss occurs near the maximum rate of change in the gradient. This consistency suggests that the initial increase in OPM neurons leads to an extreme accumulation of weight vectors (as shown in Figure 1), causing a mismatch between the structures of test and training data. The combination of this effect and the grokking effect results in an increase in test loss. However, this mismatch is eliminated after grokking, when more NPM neurons are activated, and the weight vectors relax to a broader region of directions.

## CONCLUSION AND DISCUSSIONS

The fundamental dynamics of learning models provide insights into their underlying mechanisms. Our analysis tools and key findings are summarized as follows: 1. We introduced the concepts of OPM and NPM neurons to distinguish between two distinct ways neurons extract and transfer information. OPM neurons transform information while preserving the order of the input sequence, leading to aggregation of weight vectors in the weight vector space and limiting information extraction. In contrast, NPM neurons transform information by altering the order of the input sequence, thus providing a high degree of freedom in information extraction. Our classification of neuron modes does not contradict the conventional concepts of linear and nonlinear learning [40, 41, 54]. We distinguish between linear and nonlinear networks based on the manner in which information is transformed, essentially differentiating linear operation from nonlinear operation, and provide effective indicators for quantitatively assessing their linearity and nonlinearity at the neuron level. While the idea of OPM and NPM neurons was initially presented in our

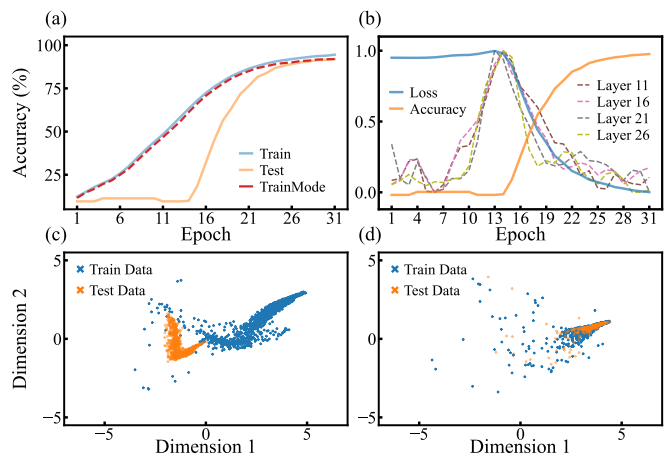


FIG. 8. Grokking Mechanism of Shallow Networks. (a) Demonstrates the grokking phenomenon. The dashed lines represent the accuracy of noisy training samples as a function of training time for various noise levels. (b) Compares the accuracy of noisy training samples and training samples with noisy weights as a function of noise amplitude, showing results from the initial stage, before grokking, and after grokking (from left to right). (c) and (d) Show two-dimensional projections of test samples for digits "0", "1", and "5" immediately before and after the grokking event, respectively. (e) and (f) Similarly, show two-dimensional projections of training samples for the same digits "0", "1", and "5" immediately before and after the grokking event, respectively.

earlier studies [55] (Other methods to characterize OPM and NPM neurons have also been attempted), our understanding has evolved, recognizing NPM's crucial role in maximum information extraction for both linearly separable and inseparable sample sets. Neuron modes analysis method has been applied in a shallow network trained by a non-backpropagation algorithm (Please refer to the supplementary materials.)

We utilized the RPD to quantify the proportion of OPM and NPM neurons in a hidden layer. Furthermore, we adopted LP to evaluate the linear separability of samples in the outputs of a hidden layer, which assesses the degree of separation among sample classes following transformations by the earlier layers. Additionally, we employed the L-map pruning to characterize the impact of linearization in the subsequent layers, specifically monitoring the degree of linearity in these layers.

2. We introduced attraction basins in both the sample vector space and the weight vector space. The size of attraction basins in the sample vector space reflects the model's generalization ability to samples, while the size of attraction basins in the weight vector space indicates the structural stability of the learning model. The concept of attraction basins in the sample vector space originates from asymmetric Hopfield neural networks [49–51].

3. Utilizing these concepts and tools, we discovered that DNNs self-organize into a standard structure, char-

acterized by a decrease in NPM neurons as depth increases, potentially culminating in purely OPM neurons in the deepest layers. The proportion of OPM and NPM neurons evolves during training: initially, OPM neurons are predominant. For smaller, well-linearly separable datasets, achieving the learning objective may solely necessitate OPM neurons. However, with larger datasets, a transition to a mixed phase of OPM and NPM neurons occurs, with the highest concentration of NPM neurons found in the first layer. The activation of NPM neurons in this initial layer facilitates the extraction of information from a broader range of directions within the weight vector space. This standard structure provides insights into layer pruning. Specifically, LP pruning can be applied to earlier layers compared to L-map pruning, as the samples become well-linearly separable before the layers reach pure linearity.

4. The expansion of the attraction basin in the sample vector space as a result of increasing network depth and width underscores a general advantage of DNNs. This effect can be grasped by conceptualizing layers as iterative operations, leading to a significant expansion of the attraction basin compared to shallow networks. Hence, our assessment of why depth enhances generalization ability hinges on this expansion of the basin of attraction. Conversely, we identified contrasting dependencies of attraction basins on depth and width in the weight vector space. This suggests that increasing either the depth or width of the network may not promote structural stability.

On the other hand, various techniques employed in DNNs, such as selecting a smaller sample batch size, utilizing an appropriate learning rate, and applying suitable regularization, can expand the basin of attraction in both the sample vector space and the weight space. This enables DNNs to retain their superior generalization capability while gaining structural stability. This offers a fresh perspective on the role of methods and strategies widely used in DNNs. The size of the attraction basin is directly correlated with the flatness of minima, providing a straightforward metric for assessing the flat minima effect.

The optimal DNN configuration necessitates a balanced depth and width. For the MNIST dataset, a DNN with 8-9 layers is deemed optimal in terms of depth. This is also a critical layer number for a DNN with longer depth. Around this depth, attraction basins in both the sample vector space and weight vector space converge, accompanied by a transition from layers with NPM neurons to layers with purely OPM neurons. The RPD analysis revealed that, for a DNN with the optimal number of layers, the proportion of NPM neurons in the first hidden layer is the highest, indicating maximum information extraction at this depth. This represents another pivotal advantage of DNNs. In other words, it is only by introducing the degree of depth as a free parameter

that we can achieve the state of maximizing information extraction for the first layer. Subsequent linear layers after the critical layer neither affect DNN accuracy nor the attraction basins but reduce the NPM neuron ratio in the first layer and slightly decrease accuracy. These findings further suggest that the key advantages of DNNs are attributable to NPM neurons, while an analysis based solely on LNNs may fail to capture these characteristics.

5. The attraction basin provides a cohesive framework for interpreting the phenomenon of "grokking" across diverse learning models and conditions. Characterized by a crossover transition during the learning process, grokking signifies a shift where test samples transition from lying outside the attraction basins of the training samples to within them. This manifestation may be observable in shallow networks, where test samples can be perceived as minor variations of the training samples. However, in deeper DNNs, the attraction basin in the sample vector space is sufficiently large, often encompassing test samples upon their establishment. When the weights of the DNN are perturbed in specific manners, such as through the evolutionary mode of Batch Normalization, test samples may initially lie outside the attraction basins but eventually converge into them, marking the occurrence of grokking. The observability of this phenomenon hinges on the size of the attraction basin and the sharpness of its boundaries. Consequently, the underlying mechanisms of grokking may diverge between deep and shallow networks. In shallow networks, it is associated with the basin of attraction in the sample vector space, whereas in deeper DNNs, it relates to the basin of attraction in the weight vector space. The double descent observed in test loss during the training process can be interpreted as a resultant effect of shifts in both the attraction basin and neuron activation modes.

6. Residual connections play a crucial role in maintaining the standard structure. As illustrated in Figure 9, residual connections empower networks to uphold stable standard structures across a vast range of depths and widths, thus equipping them with the capacity to manage large-scale datasets efficiently. DNNs endowed with residual connections are capable of achieving a standard structure across a broader spectrum of network scales compared to those devoid of residual connections.

7. In Figure 10, we depict the pruning accuracy of the L-map on the training set for various later layers in a 23-layer DNN as a function of training time. Notably, the pruning accuracy rapidly converges to the training accuracy shortly after the grokking point. This observation implies that the learning phase preceding grokking involves a gradual elimination of network noise (weight noise), akin to a "entering meditation" process.

**Statement of Author Contributions.** Specifically, Y.C.L. was responsible for performing the calculations and preparing the figures presented in this paper. Y.Z. conducted an extensive literature review and

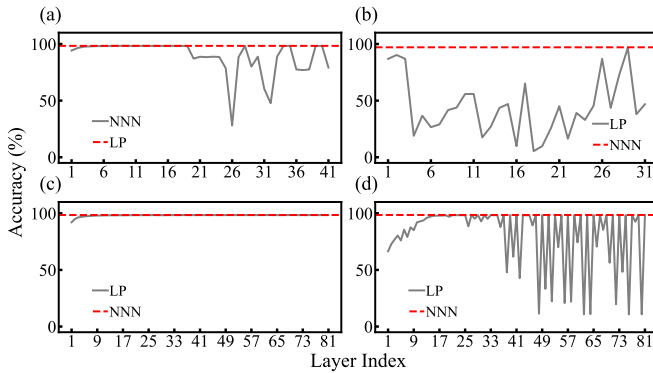


FIG. 9. Residual connections enable the maintenance of standard structures across a broader range of widths and depths. (a) A 43-layer DNN with a width of 256 without residual connections, (b) A 33-layer DNN with a width of 2048 without residual connections, (c) An 83-layer DNN with a width of 256 with residual connections, and (d) An 83-layer DNN with a width of 2048 with residual connections.

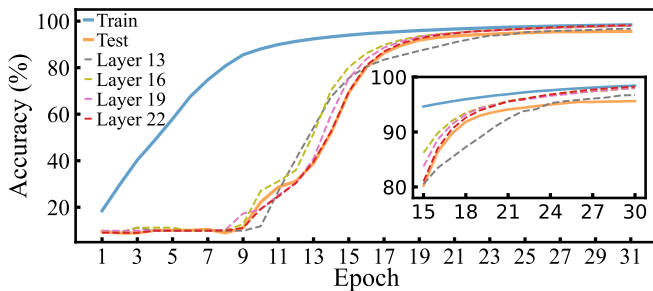


FIG. 10. The "entering meditation" effect

provided valuable insights during the analysis and discussion stages. S.H.F. carried out the initial exploratory research. Lastly, H.Z. proposed the concept of classifying neuron modes and introduced the idea of utilizing the basin of attraction for analyzing deep mechanisms. Additionally, H.Z. wrote the manuscript.

\* These authors contributed equally to this work.

† zhaoh@xmu.edu.cn

- [1] H. Mhaskar and T. Poggio, *Deep vs. shallow networks : An approximation theory perspective* (2016), [arXiv:1608.03287 \[cs.LG\]](https://arxiv.org/abs/1608.03287).
- [2] H. Mhaskar, Q. Liao, and T. Poggio, in *Proceedings of the Thirty-First AAAI Conference on Artificial Intelligence*, AAAI'17 (AAAI Press, 2017) p. 2343–2349.
- [3] T. Poggio, H. Mhaskar, L. Rosasco, B. Miranda, and Q. Liao, *Why and when can deep – but not shallow – networks avoid the curse of dimensionality: a review* (2017), [arXiv:1611.00740 \[cs.LG\]](https://arxiv.org/abs/1611.00740).
- [4] C. Zhang, S. Bengio, M. Hardt, B. Recht, and O. Vinyals, *Commun. ACM* **64**, 107–115 (2021).
- [5] T. Poggio, A. Banburski, and Q. Liao, *Proceedings of*

*the National Academy of Sciences* **117**, 30039 (2020), <https://www.pnas.org/doi/pdf/10.1073/pnas.1907369117>.

- [6] A. Vaswani, N. Shazeer, N. Parmar, J. Uszkoreit, L. Jones, A. N. Gomez, L. Kaiser, and I. Polosukhin, in *Proceedings of the 31st International Conference on Neural Information Processing Systems*, NIPS'17 (Curran Associates Inc., Red Hook, NY, USA, 2017) p. 6000–6010.
- [7] F. He and D. Tao, *Recent advances in deep learning theory* (2021), [arXiv:2012.10931 \[cs.LG\]](https://arxiv.org/abs/2012.10931).
- [8] N. Suh and G. Cheng, *A survey on statistical theory of deep learning: Approximation, training dynamics, and generative models* (2024), [arXiv:2401.07187 \[stat.ML\]](https://arxiv.org/abs/2401.07187).
- [9] N. Tishby and N. Zaslavsky, in *2015 IEEE Information Theory Workshop (ITW)* (2015) pp. 1–5.
- [10] A. A. Alemi, I. Fischer, J. V. Dillon, and K. Murphy, in *International Conference on Learning Representations* (2017).
- [11] R. Shwartz-Ziv, *Information flow in deep neural networks* (2022), [arXiv:2202.06749 \[cs.LG\]](https://arxiv.org/abs/2202.06749).
- [12] K. A. Murphy and D. S. Bassett, *Phys. Rev. Lett.* **132**, 197201 (2024).
- [13] S. Jastrzebski, Z. Kenton, D. Arpit, N. Ballas, A. Fischer, Y. Bengio, and A. Storkey, *arXiv preprint arXiv:1711.04623* (2017).
- [14] C. Ma and L. Ying, in *Advances in Neural Information Processing Systems*, edited by A. Beygelzimer, Y. Dauphin, P. Liang, and J. W. Vaughan (2021).
- [15] Y. Feng and Y. Tu, *Proceedings of the National Academy of Sciences* **118**, e2015617118 (2021), <https://www.pnas.org/doi/pdf/10.1073/pnas.2015617118>.
- [16] N. Yang, C. Tang, and Y. Tu, *Phys. Rev. Lett.* **130**, 237101 (2023).
- [17] H. Levine and Y. Tu, *Proceedings of the National Academy of Sciences* **121**, e2403580121 (2024), <https://www.pnas.org/doi/pdf/10.1073/pnas.2403580121>.
- [18] Y. Feng and Y. Tu, *The activity-weight duality in feed forward neural networks: The geometric determinants of generalization* (2023), [arXiv:2203.10736 \[cs.LG\]](https://arxiv.org/abs/2203.10736).
- [19] A. Jacot, F. Gabriel, and C. Hongler, in *Proceedings of the 32nd International Conference on Neural Information Processing Systems*, NIPS'18 (Curran Associates Inc., Red Hook, NY, USA, 2018) p. 8580–8589.
- [20] S. Arora, S. S. Du, W. Hu, Z. Li, R. Salakhutdinov, and R. Wang, *On exact computation with an infinitely wide neural net*, in *Proceedings of the 33rd International Conference on Neural Information Processing Systems* (Curran Associates Inc., Red Hook, NY, USA, 2019).
- [21] A. Saxe, J. McClelland, and S. Ganguli, in *International Conference on Learning Representations 2014* (2014).
- [22] Z. Ji and M. Telgarsky, in *International Conference on Learning Representations* (2019).
- [23] Y. Dandi, F. Krzakala, B. Loureiro, L. Pesce, and L. Stephan, *How two-layer neural networks learn, one (giant) step at a time* (2023), [arXiv:2305.18270 \[stat.ML\]](https://arxiv.org/abs/2305.18270).
- [24] T. Luo, Z.-Q. J. Xu, Z. Ma, and Y. Zhang, *J. Mach. Learn. Res.* **22** (2021).
- [25] Y. Xu and L. Ziyin, *Three mechanisms of feature learning in the exact solution of a latent variable model* (2024), [arXiv:2401.07085 \[cs.LG\]](https://arxiv.org/abs/2401.07085).
- [26] M. Geiger, L. Petrini, and M. Wyart, *Physics Reports* **924**, 1 (2021), *landscape and training regimes in deep learning*.
- [27] Y. LeCun, J. Denker, and S. Solla, in *Advances in Neu-*

- ral Information Processing Systems*, Vol. 2, edited by D. Touretzky (Morgan-Kaufmann, 1989).
- [28] F. Dalvi, H. Sajjad, N. Durrani, and Y. Belinkov, in *Proceedings of the 2020 Conference on Empirical Methods in Natural Language Processing (EMNLP)*, edited by B. Webber, T. Cohn, Y. He, and Y. Liu (Association for Computational Linguistics, Online, 2020) pp. 4908–4926.
- [29] S. Vadera and S. Ameen, *IEEE Access* **10**, 63280 (2022).
- [30] S. He, G. Sun, Z. Shen, and A. Li, *What matters in transformers? not all attention is needed* (2024), [arXiv:2406.15786 \[cs.LG\]](https://arxiv.org/abs/2406.15786).
- [31] A. Gromov, K. Tirumala, H. Shapourian, P. Gloriosi, and D. A. Roberts, *The unreasonable ineffectiveness of the deeper layers* (2024), [arXiv:2403.17887 \[cs.CL\]](https://arxiv.org/abs/2403.17887).
- [32] X. Men, M. Xu, Q. Zhang, B. Wang, H. Lin, Y. Lu, X. Han, and W. Chen, *Shortgpt: Layers in large language models are more redundant than you expect* (2024), [arXiv:2403.03853 \[cs.CL\]](https://arxiv.org/abs/2403.03853).
- [33] K. He, X. Zhang, S. Ren, and J. Sun, in *2016 IEEE Conference on Computer Vision and Pattern Recognition (CVPR)* (2016) pp. 770–778.
- [34] K. He, X. Zhang, S. Ren, and J. Sun, in *Computer Vision—ECCV 2016: 14th European Conference, Amsterdam, The Netherlands, October 11–14, 2016, Proceedings, Part IV 14* (Springer, 2016) pp. 630–645.
- [35] M. Hardt and T. Ma, in *International Conference on Learning Representations* (2017).
- [36] H. Li, Z. Xu, G. Taylor, C. Studer, and T. Goldstein, in *Proceedings of the 32nd International Conference on Neural Information Processing Systems, NIPS’18* (Curran Associates Inc., Red Hook, NY, USA, 2018) p. 6391–6401.
- [37] A. Veit, M. Wilber, and S. Belongie, in *Proceedings of the 30th International Conference on Neural Information Processing Systems, NIPS’16* (Curran Associates Inc., Red Hook, NY, USA, 2016) p. 550–558.
- [38] A. Power, Y. Burda, H. Edwards, I. Babuschkin, and V. Misra, *Grokking: Generalization beyond overfitting on small algorithmic datasets* (2022), [arXiv:2201.02177 \[cs.LG\]](https://arxiv.org/abs/2201.02177).
- [39] M. Belkin, D. Hsu, S. Ma, and S. Mandal, *Proceedings of the National Academy of Sciences* **116**, 15849 (2019), <https://www.pnas.org/doi/pdf/10.1073/pnas.1903070116>.
- [40] T. Kumar, B. Bordelon, S. J. Gershman, and C. Pehlevan, in *The Twelfth International Conference on Learning Representations* (2024).
- [41] R. Schaeffer, Z. Robertson, A. Boopathy, M. Khona, K. Pistunova, J. W. Rocks, I. R. Fiete, A. Gromov, and S. Koyejo, in *The Third Blogpost Track at ICLR 2024* (2024).
- [42] P. Nakkiran, G. Kaplun, Y. Bansal, T. Yang, B. Barak, and I. Sutskever, in *International Conference on Learning Representations* (2020).
- [43] A. Yom Din, T. Karidi, L. Choshen, and M. Geva, in *Proceedings of the 2024 Joint International Conference on Computational Linguistics, Language Resources and Evaluation (LREC-COLING 2024)*, edited by N. Calzolari, M.-Y. Kan, V. Hoste, A. Lenci, S. Sakti, and N. Xue (ELRA and ICCL, Torino, Italia, 2024) pp. 9615–9625.
- [44] N. Belrose, Z. Furman, L. Smith, D. Halawi, I. Ostrovsky, L. McKinney, S. Biderman, and J. Steinhardt, *Eliciting latent predictions from transformers with the tuned lens* (2023), [arXiv:2303.08112 \[cs.LG\]](https://arxiv.org/abs/2303.08112).
- [45] K. Pal, J. Sun, A. Yuan, B. Wallace, and D. Bau, in *Proceedings of the 27th Conference on Computational Natural Language Learning (CoNLL)*, edited by J. Jiang, D. Reitter, and S. Deng (Association for Computational Linguistics, Singapore, 2023) pp. 548–560.
- [46] A. D. Seshadri, in *Findings of the Association for Computational Linguistics: EMNLP 2024*, edited by Y. Al-Onaizan, M. Bansal, and Y.-N. Chen (Association for Computational Linguistics, Miami, Florida, USA, 2024) pp. 5187–5192.
- [47] L. Deng, *IEEE Signal Processing Magazine* **29**, 141 (2012).
- [48] Z. Liu, E. J. Michaud, and M. Tegmark, *Omnigrok: Grokking beyond algorithmic data* (2023), [arXiv:2210.01117 \[cs.LG\]](https://arxiv.org/abs/2210.01117).
- [49] H. Zhao, *Phys. Rev. E* **70**, 066137 (2004).
- [50] Q. Zhou, T. Jin, and H. Zhao, *Neural Computation* **21**, 2931 (2009).
- [51] T. Jin and H. Zhao, *Phys. Rev. E* **72**, 066111 (2005).
- [52] S. Ioffe and C. Szegedy, in *Proceedings of the 32nd International Conference on International Conference on Machine Learning - Volume 37, ICML’15 (JMLR.org, 2015)* p. 448–456.
- [53] A. Paszke, S. Gross, F. Massa, A. Lerer, J. Bradbury, G. Chanan, T. Killeen, Z. Lin, N. Gimelshein, L. Antiga, A. Desmaison, A. Kopf, E. Yang, Z. DeVito, M. Raison, A. Tejani, S. Chilamkurthy, B. Steiner, L. Fang, J. Bai, and S. Chintala, in *Advances in Neural Information Processing Systems*, Vol. 32, edited by H. Wallach, H. Larochelle, A. Beygelzimer, F. d’Alché-Buc, E. Fox, and R. Garnett (Curran Associates, Inc., 2019).
- [54] M. Geiger, S. Spigler, A. Jacot, and M. Wyart, *Journal of Statistical Mechanics: Theory and Experiment* **2020**, 113301 (2020).
- [55] S. Feng, Y. Zhang, F. Wang, and H. Zhao, *How and what to learn: the modes of machine learning* (2022), [arXiv:2202.13829 \[cs.LG\]](https://arxiv.org/abs/2202.13829).